Dynamics of entanglement asymmetry for space-inversion symmetry of free fermions on honeycomb lattices

Ryogo Hara,^{1,*} Shimpei Endo,¹ and Shion Yamashika^{1,†}

¹Department of Engineering Science, University of Electro-Communications, Chofu, Tokyo 182-8585, Japan

We study the entanglement asymmetry for the space-inversion symmetry of free fermions on a twodimensional honeycomb lattice with an on-site energy imbalance between the two sublattices. We show that the entanglement asymmetry of a local subsystem exhibits nonanalytic dependence on the energy imbalance, due to the presence of Dirac points in the Brillouin zone. We also study the quench dynamics from the ground state into the inversion-symmetric point at which the energy imbalance vanishes. Under certain conditions on the subsystem geometry, the entanglement asymmetry relaxes to a finite value after the quench, revealing that the inversion-symmetry breaking in the initial ground state can persist even under the symmetric dynamics. We attribute the absence of symmetry restoration to the presence of a flat energy dispersion (flat band) in a specific direction.

I. INTRODUCTION

Nonequilibrium quantum many-body systems have attracted considerable attention for decades, as they display rich phenomena absent in equilibrium, and provide a setting to address central questions at the interface between quantum and statistical physics [1–4]. Although an isolated quantum system evolves unitarily and never approaches a stationary state, a local subsystem embedded in the whole system often relaxes into a statistical ensemble, which is typically a Gibbs ensemble in generic cases [5–17] or, in integrable systems, a generalized Gibbs ensemble (GGE) [18–26]. Clarifying when and how this effective equilibration occurs, and when it fails, is essential for a microscopic understanding of statistical mechanics.

Quantum quenches provide a simple and controllable way to drive an isolated quantum system out of equilibrium. In this protocol, the system is initially prepared in the ground state of a given Hamiltonian and then evolves unitarily after a sudden change of its parameters. This setup has been widely used to study the relaxation dynamics of isolated quantum systems, including experimental realizations in trapped ion [27–29] and cold atom [9, 30–32] systems. A standard diagnostic in quantifying the relaxation dynamics following a quantum quench is the entanglement entropy, defined as the von Neumann entropy of a local subsystem [33–36]. After a quench, it typically grows linearly in time and then approaches a stationary value equal to that of the corresponding statistical ensemble, signaling the equilibration at the subsystem level [37-39].

The entanglement asymmetry has been introduced as a measure of symmetry breaking within a subsystem, providing another way to quantify the relaxation dynamics from the viewpoint of symmetry [40]: When the post-quench Hamiltonian preserves a certain symmetry while the initial state breaks it, the symmetry within a local

subsystem is typically restored after the quench, as the reduced density matrix for the subsystem relaxes into a (generalized) Gibbs ensemble of the symmetric postquench Hamiltonian. The entanglement asymmetry provides a quantitative means to analyze the rate of this symmetry restoration, leading to the discovery and subsequent extensive study on the quantum Mpemba effect, where a subsystem that initially breaks more the symmetry can restore it faster [40–60]. In addition, it has revealed counterintuitive phenomena in which the symmetry is not restored despite the symmetric dynamics [61, 62]. The entanglement asymmetry has also been investigated in several contexts apart from quench dynamics, including generic compact Lie groups in matrix product states [63, 64], critical systems described by conformal field theory [65–68], and Haar-random states that emulate evaporating black holes [69].

In contrast to one-dimensional systems, the symmetry aspects of the relaxation dynamics in higher-dimensional systems remain less understood. In particular, previous studies have mainly focused on the simplest square-lattice systems [42, 62, 70–72], and the role of lattice geometry remains an open question. Moreover, while the entanglement asymmetry has been applied to physical systems with various symmetries, including those generated by non-Abelian charges [63, 73], spatial translations [53, 74], and non-invertible symmetries [75, 76], some fundamental symmetries in condensed matter physics, such as space-inversion and time-reversal symmetries, have been unexplored in this context.

Free fermions on a honeycomb lattice offer an ideal platform to address these questions. The honeycomb lattice, consisting of two triangular sublattices, naturally admits space-inversion symmetry of exchanging the sublattices. This symmetry plays a crucial role in the low-energy band structure of the system: When the inversion symmetry is preserved, the energy spectrum exhibits gapless linear dispersions at the corners of the Brillouin zone (the Dirac points), yielding massless low-energy quasiparticle excitations [77, 78]. On the other hand, when the symmetry is broken, for example by introducing an energy imbalance between sublattices, a gap opens and

^{*} r.hara-phys@uec.ac.jp

[†] shion.yamashika@uec.ac.jp

quasiparticles acquire an effective mass [79]. This characteristic physics, first realized in graphene [80, 81], has stimulated extensive research into relativistic-like quasiparticles in condensed matter and emergent topological phenomena such as the quantum Hall effect [77, 82–84]. In addition to electronic systems, the honeycomb lattice system has been realized in ultracold atoms in optical lattices [85–87], photonic systems [88–91], and mechanical metamaterials [92, 93].

In this paper, we study the quench dynamics of the entanglement asymmetry associated with the spaceinversion symmetry in spinless (i.e., spin-polarized) free fermions on a honeycomb lattice. We derive analytical expressions for the time evolution of the entanglement asymmetry in the quench dynamics starting from the ground state of the Hamiltonian with the on-site energy imbalance between the sublattices into the inversionsymmetric Hamiltonian without the imbalance. When size of the subsystem, taken as a periodic stripe shape, is odd in the periodic direction, the entanglement asymmetry tends to zero and the inversion symmetry is restored after the quench, as the subsystem relaxes into the GGE of the inversion-symmetric post-quench Hamiltonian. In contrast, when the subsystem size is even, the entanglement asymmetry relaxes to a finite value, indicating the absence of inversion-symmetry restoration. We attribute this absence of symmetry restoration to a macroscopic occupation of quasiparticle modes with zero group velocity (i.e., flat band), demonstrating the crucial role of band structures in the relaxation dynamics.

This paper is organized as follows. In Sec. II, we introduce our quench protocol and define the entanglement asymmetry for the space-inversion symmetry. In Sec. III, we describe the method to calculate the entanglement asymmetry in the two-dimensional system. In Sec. IV, we analyze the entanglement asymmetry in the ground state of the Hamiltonian with the on-site energy imbalance between sublattices. In Sec. V, we examine its time evolution after the quench and show that, in certain cases, the inversion symmetry is not restored even in the large time limit. In Sec. VI, we identify the physical mechanism responsible for the absence of inversion-symmetry restoration. Section VII summarizes our results. Appendixes provide technical details and derivations of several formulas used in the main text. We set $\hbar = 1$ and lattice constant unity throughout this paper.

II. SYSTEM SETUP AND DEFINITIONS OF ENTANGLEMENT ASYMMETRY

We consider free fermions on a honeycomb lattice consisting of triangular sublattices Λ_A and Λ_B . For convenience, we perform the lattice transformation from the honeycomb lattice to a brickwork lattice as shown in Fig. 1, which does not change the lattice topology. The

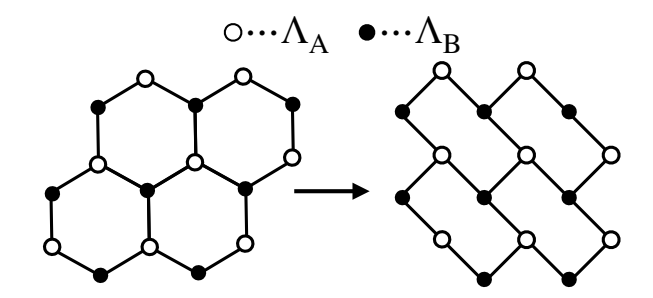


FIG. 1. Schematic illustration of the transformation from the honeycomb to the brickwork lattices.

system is described by the following Hamiltonian

$$H_{0} = -J \sum_{\mathbf{i} \in \Lambda_{A}} \sum_{\nu=1,2,3} (a_{\mathbf{i}}^{\dagger} b_{\mathbf{i}+\mathbf{d}_{\nu}} + \text{H.c.})$$

$$+ M \sum_{\mathbf{i} \in \Lambda_{A}} a_{\mathbf{i}}^{\dagger} a_{\mathbf{i}} - M \sum_{\mathbf{i} \in \Lambda_{B}} b_{\mathbf{i}}^{\dagger} b_{\mathbf{i}}, \quad (1)$$

where $a_{\bf i}$ ($b_{\bf i}$) is the annihilation operator of a fermion on ${\bf i} \in \Lambda_{\rm A(B)}$, ${\bf i} = (i_x, i_y)$ is the two-dimensional vector identifying the position of the site, J>0 is the hopping amplitude between nearest-neighbor sites, M is the onsite energy difference between the two sublattices, and ${\bf d}_{\nu}$ ($\nu=1,2,3$) are the nearest-neighbor vectors that are defined as (we take the lattice constant as a unit of length)

$$\mathbf{d}_1 = \frac{1}{2} \begin{pmatrix} 1 \\ -1 \end{pmatrix}, \mathbf{d}_2 = \frac{1}{2} \begin{pmatrix} -1 \\ 1 \end{pmatrix}, \mathbf{d}_3 = \frac{1}{2} \begin{pmatrix} -1 \\ -1 \end{pmatrix}.$$
 (2)

We denote as $L_{x(y)}$ the length of the system in the longitudinal (transverse) direction. The periodic boundary conditions are imposed along both directions. When M/J=0, the Hamiltonian (1) is invariant under the space-inversion \mathcal{P} that exchanges sublattices $\Lambda_{\rm A}$ and $\Lambda_{\rm B}$ as $\mathcal{P}a_{\bf i}\mathcal{P}^{-1}=b_{-\bf i}$ and $\mathcal{P}b_{\bf i}\mathcal{P}^{-1}=a_{-\bf i}$, whereas this inversion symmetry is broken for $M/J\neq 0$. The inversion-symmetry breaking changes the energy spectrum of the Hamiltonian (1) from gapless to gapped, as we will see below.

Performing the Fourier transformations

$$a_{\mathbf{i}} = \frac{1}{\sqrt{L_x L_y}} \sum_{\mathbf{k}} e^{i\mathbf{k} \cdot \mathbf{i}} a_{\mathbf{k}}, \tag{3}$$

$$b_{\mathbf{i}} = \frac{1}{\sqrt{L_x L_y}} \sum_{\mathbf{k}} e^{i\mathbf{k} \cdot \mathbf{i}} b_{\mathbf{k}}, \tag{4}$$

where $\mathbf{k}=(k_x,k_y)$ with $k_{x(y)}=2\pi n_{x(y)}/L_{x(y)}$ $(n_{x(y)}=0,...,L_{x(y)}-1),$ the Hamiltonian (1) reduces to

$$H_{0} = -J \sum_{\mathbf{k}} (a_{\mathbf{k}}^{\dagger}, b_{\mathbf{k}}^{\dagger}) \begin{bmatrix} -M/J & \sum_{\nu=1}^{3} e^{i\mathbf{k} \cdot \mathbf{d}_{\nu}} \\ \sum_{\nu=1}^{3} e^{-i\mathbf{k} \cdot \mathbf{d}_{\nu}} & M/J \end{bmatrix} \begin{pmatrix} a_{\mathbf{k}} \\ b_{\mathbf{k}} \end{pmatrix}. (5)$$

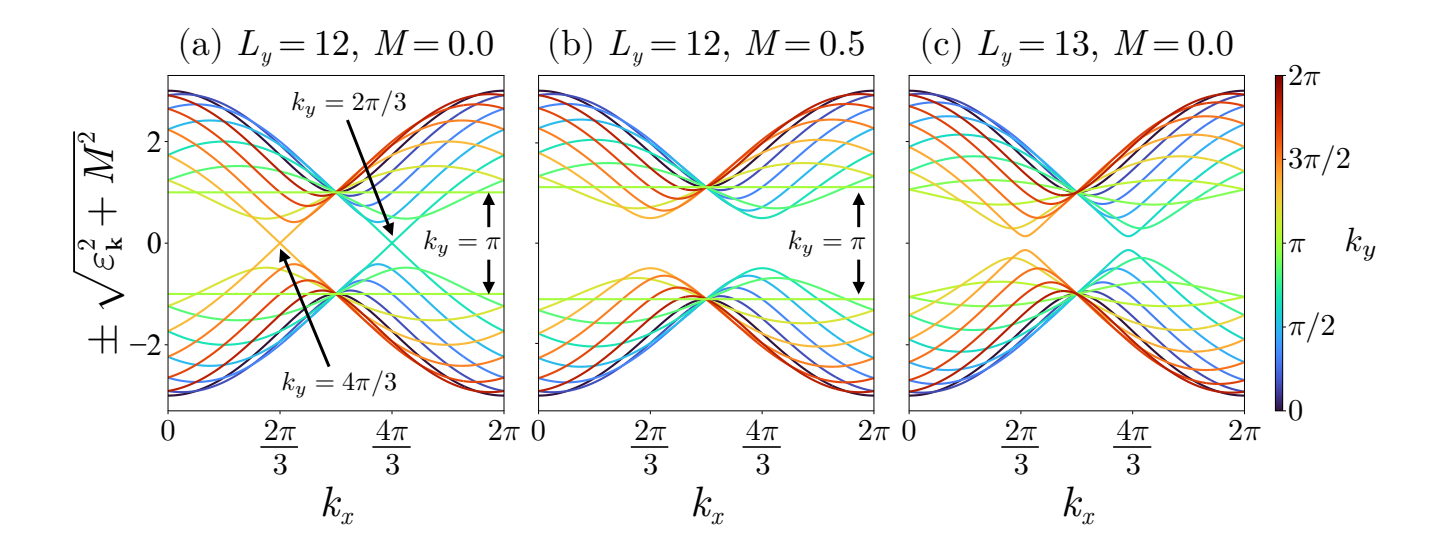


FIG. 2. The energy spectra of the Hamiltonian in Eq. (1) for several fixed values of L_y . We set J=1 in all the plots.

It can be diagonalized by the linear transformation

$$\begin{pmatrix} \alpha_{\mathbf{k}} \\ \beta_{\mathbf{k}} \end{pmatrix} = \begin{pmatrix} e^{\mathrm{i}\frac{\phi_{\mathbf{k}}}{2}} \cos\frac{\theta_{\mathbf{k}}}{2} & e^{-\mathrm{i}\frac{\phi_{\mathbf{k}}}{2}} \sin\frac{\theta_{\mathbf{k}}}{2} \\ -e^{\mathrm{i}\frac{\phi_{\mathbf{k}}}{2}} \sin\frac{\theta_{\mathbf{k}}}{2} & e^{-\mathrm{i}\frac{\phi_{\mathbf{k}}}{2}} \cos\frac{\theta_{\mathbf{k}}}{2} \end{pmatrix} \begin{pmatrix} a_{\mathbf{k}} \\ b_{\mathbf{k}} \end{pmatrix}, \quad (6)$$

where the angles $(\theta_{\mathbf{k}}, \phi_{\mathbf{k}})$ are determined by

$$\cos \theta_{\mathbf{k}} = \frac{M}{\sqrt{\varepsilon_{\mathbf{k}}^2 + M^2}},\tag{7}$$

$$\sin \theta_{\mathbf{k}} \cos \phi_{\mathbf{k}} = -\frac{J \sum_{\nu=1}^{3} \cos(\mathbf{k} \cdot \mathbf{d}_{\nu})}{\sqrt{\varepsilon_{\mathbf{k}}^{2} + M^{2}}}, \tag{8}$$

$$\sin \theta_{\mathbf{k}} \sin \phi_{\mathbf{k}} = \frac{J \sum_{\nu=1}^{3} \sin(\mathbf{k} \cdot \mathbf{d}_{\nu})}{\sqrt{\varepsilon_{\mathbf{k}}^{2} + M^{2}}},$$
 (9)

with

$$\varepsilon_{\mathbf{k}} = J \left| \sum_{\nu=1}^{3} e^{i\mathbf{k} \cdot \mathbf{d}_{\nu}} \right|. \tag{10}$$

Substituting Eq. (6) into Eq. (5), we obtain

$$H_0 = \sum_{\mathbf{k}} \sqrt{\varepsilon_{\mathbf{k}}^2 + M^2} (\alpha_{\mathbf{k}}^{\dagger} \alpha_{\mathbf{k}} - \beta_{\mathbf{k}}^{\dagger} \beta_{\mathbf{k}}). \tag{11}$$

The above expression shows that the energy spectrum of the Hamiltonian consists of upper and lower bands with dispersions $+\sqrt{\varepsilon_{\mathbf{k}}^2+M^2}$ and $-\sqrt{\varepsilon_{\mathbf{k}}^2+M^2}$, respectively, and that $\alpha_{\mathbf{k}}$ and $\beta_{\mathbf{k}}$ correspond to the quasiparticle operators associated with these bands. If we denote as $|\Psi_0\rangle$ the ground state of the Hamiltonian (11) at half filling, it corresponds to the fully occupied lower band and the empty upper band, i.e.,

$$|\Psi_0\rangle = \prod_{\mathbf{k}} \beta_{\mathbf{k}}^{\dagger} |0\rangle ,$$
 (12)

where $|0\rangle$ is the fermionic vacuum state annihilated by $a_{\mathbf{i}}$ and $b_{\mathbf{i}}$, i.e., $a_{\mathbf{i}} |0\rangle = b_{\mathbf{i}} |0\rangle = 0 \ \forall \mathbf{i}$.

Figure 2 shows the energy spectra of the Hamiltonian (11). As shown in Fig. 2 (a), when M=0 and L_y is a multiple of three, linear dispersions appear around the Dirac points $\mathbf{k}=\pm(2\pi/3,4\pi/3)$ [77], where $-k_{x(y)}$ and $2\pi-k_{x(y)}$ are equivalent because of the periodicity of the Brillouin zone. As seen in Fig. 2 (b), a gap opens when $M\neq 0$ as a consequence of inversion-symmetry breaking [79]. Even when M=0, a gap opens if L_y is not divisible by three because the quantized momenta \mathbf{k} do not take the Dirac points, as shown in Fig. 2 (c). We also find in Figs. 2 (a) and (b) that $\varepsilon_{\mathbf{k}}$ with fixed $k_y=\pi$ becomes independent of k_x , which occurs only when L_y is even. The presence of the flat dispersion relation in the k_x -direction critically affects the relaxation dynamics after a quantum quench, as shown in Secs. V and VI.

We study the dynamical behavior of inversion-symmetry breaking following the global quantum quench from an asymmetric point $M \neq 0$ into the symmetric point M=0. After the quench, the system is described by the time-evolved state $|\Psi_t\rangle = e^{-\mathrm{i}tH}\,|\Psi_0\rangle$, where $|\Psi_0\rangle$ and H are the initial ground state given in Eq. (12) and the post-quench Hamiltonian that is obtained by setting M=0 into Eq. (1), respectively. The post-quench Hamiltonian specifically reads

$$H = \sum_{\mathbf{k}} \varepsilon_{\mathbf{k}} (\gamma_{\mathbf{k}+}^{\dagger} \gamma_{\mathbf{k}+} - \gamma_{\mathbf{k}-}^{\dagger} \gamma_{\mathbf{k}-}), \tag{13}$$

with

$$\begin{pmatrix} \gamma_{\mathbf{k}+} \\ \gamma_{\mathbf{k}-} \end{pmatrix} = \frac{1}{\sqrt{2}} \begin{pmatrix} e^{i\frac{\phi_{\mathbf{k}}}{2}} & e^{-i\frac{\phi_{\mathbf{k}}}{2}} \\ -e^{i\frac{\phi_{\mathbf{k}}}{2}} & e^{-i\frac{\phi_{\mathbf{k}}}{2}} \end{pmatrix} \begin{pmatrix} a_{\mathbf{k}} \\ b_{\mathbf{k}} \end{pmatrix}. \tag{14}$$

Since the post-quench Hamiltonian (13) commutes with \mathcal{P} , the degree of inversion-symmetry breaking in the

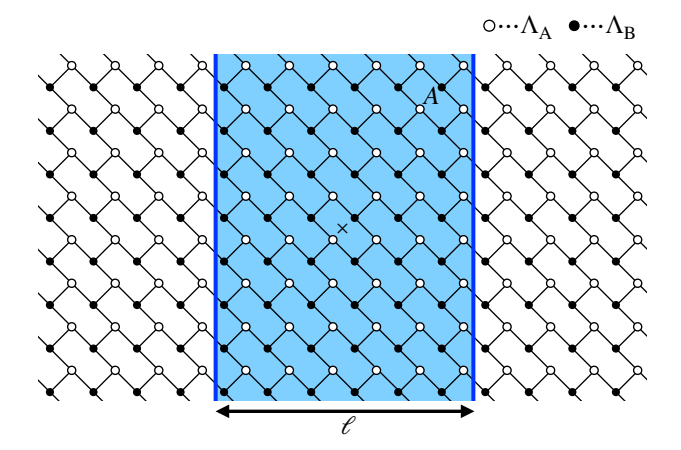


FIG. 3. Schematic illustration of the bipartition of the whole system into the subsystems. The blue region represents subsystem A and the cross symbol at the center indicates the coordinate origin.

global state $|\Psi_t\rangle$ remains unchanged from that in the initial state $|\Psi_0\rangle$. Instead, by decomposing the whole system into a local subsystem A and its complement \bar{A} , we investigate the breaking of the inversion symmetry within the subsystem. As illustrated in Fig. 3, we take as subsystem A the stripe of length ℓ with the periodic boundary condition in the transverse direction. The subsystem is described by the reduced density matrix

$$\rho_A(t) = \operatorname{Tr}_{\bar{A}}(|\Psi_t\rangle \langle \Psi_t|), \tag{15}$$

where $\operatorname{Tr}_{\bar{A}}$ stands for the partial trace over subsystem \bar{A} . To study the inversion-symmetry breaking within subsystem A, we place the spatial origin at its center (denoted as a cross symbol in Fig.3) so that the sites inside A are mapped onto sites within A under the inversion \mathcal{P} . We quantify the degree of the inversion-symmetry breaking within subsystem A by using the Rényi entanglement asymmetry that is defined as [40]

$$\Delta S_A^{(n)}(t) = \frac{1}{1-n} \ln \left(\frac{\text{Tr}[\bar{\rho}_A(t)^n]}{\text{Tr}[\rho_A(t)^n]} \right), \tag{16}$$

where n is the replica index and $\bar{\rho}_A = (\rho_A + \mathcal{P}\rho_A \mathcal{P}^{-1})/2$ is the symmetrization of ρ_A with respect to the inversion \mathcal{P} . In the limit $n \to 1$, Eq. (16) reduces to the von-Neumann entanglement asymmetry, which is the Kullback-Leibler divergence between ρ_A and $\bar{\rho}_A$, i.e.,

$$\Delta S_A^{(1)}(t) := \lim_{n \to 1} \Delta S_A^{(n)}(t)$$

= Tr[\rho_A(t)\{\log \rho_A(t) - \log \bar{\rho}_A(t)\}\]. (17)

The entanglement asymmetry has the desired properties as a measure of symmetry breaking [94, 95]: it is positive semidefinite, $\Delta S_A^{(n)} \geq 0$, and reduces to zero if and only if the reduced density matrix is symmetric, i.e., $\Delta S_A^{(n)} = 0 \Leftrightarrow \mathcal{P}\rho_A\mathcal{P}^{-1} = \rho_A$.

III. CHARGED MOMENTS AND DIMENSIONAL REDUCTION

Here, we describe the method to calculate the entanglement asymmetry by applying a dimensional reduction technique, which was originally introduced in Ref. [96] and has been employed to study the entanglement entropy of higher-dimensional systems both in and out of equilibrium [70, 97–100]. This approach exploits the translational invariance of the subsystem in one spatial direction to decompose the original two-dimensional problem into a set of independent one-dimensional ones, thereby making exact results for one-dimensional systems applicable. More recently, this framework has been extended to the entanglement asymmetry in two-dimensional square-lattice systems [42, 62]. Here, we apply it to the brickwork-lattice system corresponding to the honeycomb lattice.

Substituting $\bar{\rho}_A = (\rho_A + \mathcal{P}\rho_A \mathcal{P}^{-1})/2$ into Eq. (16), the Rényi entanglement asymmetry can be written as

$$\Delta S_A^{(n)}(t) = \frac{1}{1-n} \ln \left(\frac{1}{2^n} \sum_{\boldsymbol{\alpha} \in \{0,1\}^n} \frac{Z_n(\boldsymbol{\alpha}, t)}{Z_n(\boldsymbol{0}, t)} \right), \quad (18)$$

where $Z_n(\boldsymbol{\alpha},t)$ are the charged moments defined as

$$Z_n(\boldsymbol{\alpha}, t) = \text{Tr}\left[\prod_{j=1}^n \rho_{A, \alpha_j}(t)\right],$$
 (19)

with $\rho_{A,0} = \rho_A$ and $\rho_{A,1} = \mathcal{P}\rho_A\mathcal{P}^{-1}$. Note that, for n=2, the charged moments in Eq. (19) reduces to the overlap between two density matrices, $Z_2(\boldsymbol{\alpha}) = \text{Tr}(\rho_{A,\alpha_1}\rho_{A,\alpha_2})$, which is accessible in cold-atom experiments by using beam splitters and on-site occupation measurement [9, 32, 101, 102].

Since the initial state $|\Psi_0\rangle$ is Gaussian and the postquench Hamiltonian is quadratic, the time-evolved state $|\Psi_t\rangle$ and its reduced density matrix ρ_A are also Gaussian and satisfy Wick's theorem. In addition, as the inversion $\mathcal P$ preserves the Gaussianity of the state, the inverted reduced density matrix $\rho_{A,1} = \mathcal P \rho_A \mathcal P^{-1}$ also satisfies Wick's theorem. This implies that $\rho_{A,\alpha}$ in Eq. (19) can be univocally described by the two-point correlation matrix Γ_α whose entries are defined as [103]

$$[\Gamma_{\alpha}(t)]_{\mathbf{i},\mathbf{i}'} = 2 \operatorname{Tr}_{A}[\rho_{A,\alpha}(t) \mathbf{\Psi}_{\mathbf{i}} \mathbf{\Psi}_{\mathbf{i}'}^{\dagger}] - \delta_{\mathbf{i},\mathbf{i}'} I, \qquad (20)$$

where $\mathbf{i}, \mathbf{i}' \in A \cap \Lambda_A$ and $\Psi_{\mathbf{i}} = (a_{\mathbf{i}}, b_{\mathbf{i}+\mathbf{d}_2})^T$. Evaluating the correlators in Eq. (20) with the time-evolved state $\mathcal{P}^{\alpha} |\Psi_t\rangle$, we obtain

$$[\Gamma_{\alpha}(t)]_{\mathbf{i},\mathbf{i}'} = \frac{1}{L_x L_y} \sum_{\mathbf{k}} e^{i\mathbf{k} \cdot (\mathbf{i} - \mathbf{i}')} \mathcal{G}_{\mathbf{k},\alpha}(t), \qquad (21)$$

where $\mathcal{G}_{\mathbf{k},\alpha}$ is the 2×2 matrix defined as

$$\mathcal{G}_{\mathbf{k},\alpha}(t) = e^{-\frac{i}{2}(\mathbf{k}\cdot\mathbf{d}_2 + \phi_{\mathbf{k}})\sigma_z} [\sigma_x \sin\theta_{\mathbf{k}} + (-1)^{\alpha}\sigma_z \cos\theta_{\mathbf{k}} e^{2it\varepsilon_{\mathbf{k}}\sigma_x}] e^{\frac{i}{2}(\mathbf{k}\cdot\mathbf{d}_2 + \phi_{\mathbf{k}})\sigma_z}, \quad (22)$$

with $\sigma_{x,y,z}$ being the standard Pauli matrices. The reduced density matrix $\rho_{A,\alpha}$ can be expressed by using the two-point correlation matrix $\Gamma_{A,\alpha}$ as [103]

$$\rho_{A,\alpha}(t) = \det\left(\frac{I + \Gamma_{\alpha}(t)}{2}\right) \times \exp\left(\sum_{\mathbf{i}, \mathbf{i}' \in A \cap \Lambda_{A}} \mathbf{\Psi}_{\mathbf{i}}^{\dagger} \log\left(\frac{I - \Gamma_{\alpha}(t)}{I + \Gamma_{\alpha}(t)}\right)_{\mathbf{i}, \mathbf{i}'} \mathbf{\Psi}_{\mathbf{i}'}\right). \tag{23}$$

Plugging Eq. (23) into Eq. (19) and applying the Baker-Campbell-Hausdorff formula, we obtain

$$Z_n(\boldsymbol{\alpha}, t) = \det\left(\prod_{j=1}^n \frac{I + \Gamma_{\alpha_j}(t)}{2}\right) \times \det\left(I + \prod_{j=1}^n \frac{I - \Gamma_{\alpha_j}(t)}{I + \Gamma_{\alpha_j}(t)}\right). \quad (24)$$

We give the derivation of Eq. (24) in more detail in Appendix A.

Since the global state $|\Psi_t\rangle$ is invariant under translations and subsystem A is taken to be periodic in the transverse direction, the reduced density matrix ρ_A inherits the translational symmetry in that direction. To take advantage of this in the calculation of the charged moments in Eq. (24), we introduce the unitary matrix U with entries

$$U_{(i_x, i_y), (i_x', n_y)} = \frac{\delta_{i_x, i_x'} e^{\frac{2i\pi n_y}{L_y} i_y}}{\sqrt{L_y}}.$$
 (25)

The matrix U represents the partial Fourier transform only in the transverse direction. From Eqs. (21) and (25), we obtain

$$U\Gamma_{\alpha}(t)U^{\dagger} = \bigoplus_{n_{y}=0}^{L_{y}-1} \Gamma_{\alpha,k_{y}}(t). \tag{26}$$

Here, Γ_{α,k_y} is the $2\ell \times 2\ell$ two-point correlation matrix for the one-dimensional system labeled by the transverse momentum $k_y = 2\pi n_y/L_y$. In the thermodynamic limit in the longitudinal direction, $L_x \to \infty$, Γ_{α,k_y} reduces to the block-Toeplitz matrix as

$$[\Gamma_{\alpha,k_y}(t)]_{i_x,i_x'} = \int_{-\pi}^{\pi} \frac{dk_x}{2\pi} e^{ik_x(i_x - i_x')} \mathcal{G}_{\mathbf{k},\alpha}(t), \qquad (27)$$

where the symbol $\mathcal{G}_{\mathbf{k},\alpha}$ is given in Eq. (22). Substituting identity $I = UU^{\dagger} = U^{\dagger}U$ in Eq. (24) and employing the block-diagonal structure (26), we can decompose the charged moments into the product of independent contributions of each transverse-momentum sector as

$$Z_n(\boldsymbol{\alpha}, t) = \prod_{n_y=0}^{L_y-1} Z_{n, k_y}(\boldsymbol{\alpha}, t), \tag{28}$$

where

$$Z_{n,k_y}(\boldsymbol{\alpha},t) = \det\left(\prod_{j=1}^n \frac{I + \Gamma_{\alpha_j,k_y}(t)}{2}\right)$$

$$\times \det\left(I + \prod_{j=1}^n \frac{I - \Gamma_{\alpha_j,k_y}(t)}{I + \Gamma_{\alpha_j,k_y}(t)}\right). \quad (29)$$

Note that $Z_{n,k_y}(\boldsymbol{\alpha},t)$ in the above equation are the charged moments for a one-dimensional state labeled by the transverse momentum $k_y = 2\pi n_y/L_y$. In the following sections, we derive analytical expressions for the entanglement asymmetry in the ground state and the time-evolved state by combining well-developed techniques for one-dimensional systems with Eq. (29).

IV. ENTANGLEMENT ASYMMETRY IN THE GROUND STATE OF PRE-QUENCH HAMILTONIAN

In this section, we investigate the entanglement asymmetry in the ground state of the Hamiltonian (1), which serves as the initial state of our quench protocol. In particular, we analytically calculate the asymptotic form of the entanglement asymmetry for $\ell \gg 1$ taking the thermodynamic limit in the longitudinal direction, $L_x \to \infty$.

As shown in Sec. III, the Rényi entanglement asymmetry for the ground state can be calculated from the momentum-resolved charged moments in Eq. (29) at t=0. For clarity, we first present the calculation of the charged moments for n=2. In this case, Eq. (29) at t=0 simplifies as

$$Z_{2,k_y}(\boldsymbol{\alpha},0) = \det\left(\frac{I + \Gamma_{\alpha_1,k_y}(0)\Gamma_{\alpha_2,k_y}(0)}{2}\right). \tag{30}$$

The above expression involves the product of the block-Toeplitz matrices, $\Gamma_{\alpha_1,k_y}(0)\Gamma_{\alpha_2,k_y}(0)$, which is in general not a block-Toeplitz matrix. However, for $\ell \gg 1$, the product of block-Toeplitz matrices can be approximated by the block-Toeplitz matrix generated by the product of the symbols of the factors, see e.g. Ref. [61]. This allows us to approximate Eq. (30) as

$$Z_{2,k_y}(\boldsymbol{\alpha},0) \simeq \det T[z_{2,\mathbf{k}}(\boldsymbol{\alpha})].$$
 (31)

Here, $T[z_{2,\mathbf{k}}(\boldsymbol{\alpha})]$ is the $2\ell \times 2\ell$ block-Toeplitz matrix whose elements are given by

$$T[z_{2,\mathbf{k}}(\boldsymbol{\alpha})]_{i_x i_x'} = \int_{-\pi}^{\pi} \frac{dk_x}{2\pi} e^{ik_x(i_x - i_x')} z_{2,\mathbf{k}}(\boldsymbol{\alpha}), \qquad (32)$$

with the 2×2 symbol

$$z_{2,\mathbf{k}}(\boldsymbol{\alpha}) = \frac{I + \mathcal{G}_{\mathbf{k},\alpha_1}(0)\mathcal{G}_{\mathbf{k},\alpha_2}(0)}{2}.$$
 (33)

The asymptotic form of the determinant in Eq. (31)for $\ell \gg 1$ can be evaluated using Widom-Szegő theorem [104], which results in

$$\ln \frac{Z_{2,k_y}(\boldsymbol{\alpha},0)}{Z_{2,k_y}(\boldsymbol{0},0)} \simeq \ell \int_{-\pi}^{\pi} \frac{dk_x}{2\pi} \ln \frac{\det z_{2,\mathbf{k}}(\boldsymbol{\alpha})}{\det z_{2,\mathbf{k}}(\boldsymbol{0})}$$
(34)

$$= \ell |\alpha_1 - \alpha_2| \int_{-\pi}^{\pi} \frac{dk_x}{2\pi} \ln \sin^2 \theta_{\mathbf{k}}. \tag{35}$$

As shown in Appendix B, Eq. (35) can be generalized to $n \ge 2$ as

$$\ln \frac{Z_{n,k_y}(\boldsymbol{\alpha},0)}{Z_{n,k_y}(\boldsymbol{0},0)} \simeq \ell N^{(n)}(\boldsymbol{\alpha}) \int_{-\pi}^{\pi} \frac{dk_x}{4\pi} \ln \sin^2 \theta_{\mathbf{k}}, \quad (36)$$

with $N^{(n)}(\boldsymbol{\alpha}) = \sum_{j=1}^{n} |\alpha_j - \alpha_{j+1}|$ and $\alpha_{n+1} = \alpha_1$. Applying it to Eq. (28), we obtain the charged moments

$$\frac{Z_n(\boldsymbol{\alpha},0)}{Z_n(\boldsymbol{0},0)} \simeq X_0^{N_n(\boldsymbol{\alpha})},\tag{37}$$

where

$$X_0 = \exp\left(-\ell \sum_{n_y=0}^{L_y-1} \int_{-\pi}^{\pi} \frac{dk_x}{4\pi} \ln\left(1 + \frac{M^2}{\varepsilon_{\mathbf{k}}^2}\right)\right).$$
 (38)

Here, we used $\sin^2\theta_{\bf k}=\varepsilon_{\bf k}^2/(\varepsilon_{\bf k}^2+M^2)$ from Eq. (7). Substituting Eq. (37) into Eq. (18), we obtain the Rényi entanglement asymmetry. The summation over $\alpha \in \{0,1\}^n$ in Eq. (18) can be calculated analytically, as described in Appendix C. We finally arrive at the concise expression for the Rényi entanglement asymmetry of the ground state,

$$\Delta S_A^{(n)}(0) \simeq H^{(n)}(X_0),$$
 (39)

where

$$H^{(n)}(x) = \frac{1}{1-n} \ln \left(\left[\frac{1+x}{2} \right]^n + \left[\frac{1-x}{2} \right]^n \right)$$
 (40)

denotes the Rényi entropy of order n for a single bit of information. Taking the limit $n \to 1$ in Eq. (39), we also obtain the von-Neumann entanglement asymmetry for the ground state as

$$\Delta S_1^{(1)}(0) \simeq H^{(1)}(X_0),$$
 (41)

with

$$H^{(1)}(x) := \lim_{n \to 1} H^{(n)}(x)$$

$$= -\frac{1+x}{2} \ln \frac{1+x}{2} - \frac{1-x}{2} \ln \frac{1-x}{2}.$$
(42)

In Fig. 4, we show the n=2 Rényi entanglement asymmetry of the ground state as a function of M. It shows that the analytical result in Eq. (39) agrees excellently with the exact ones obtained by numerically evaluating the momentum-resolved charged moments in Eq. (29).

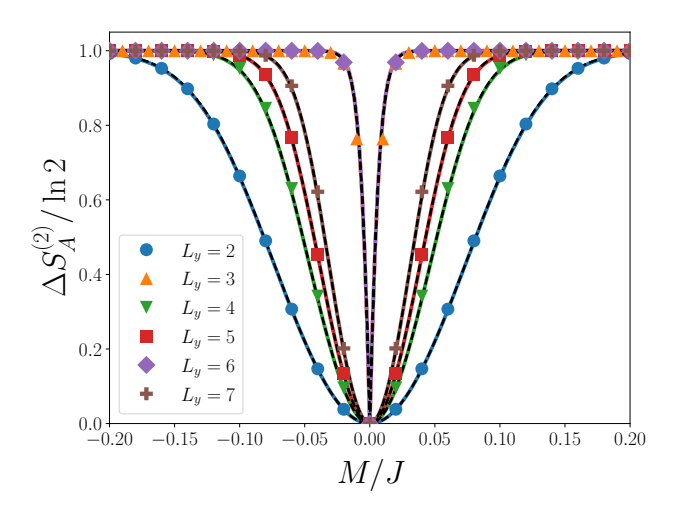


FIG. 4. The n=2 Rényi entanglement asymmetry of the ground state (12). The solid curves and symbols are the analytical result in Eq. (39) with X_0 obtained using Eq. (38) and the exact results obtained numerically by evaluating Eq. (29), respectively. The black dashed curves denote the asymptotic approximations of Eq. (39) with Eqs. (44) and (46). We take $\ell = 100$ for all the plots.

As expected, the entanglement asymmetry decreases as |M/J| gets smaller and vanishes at the symmetric point M/J=0. For large |M/J|, the entanglement asymmetry saturates to the maximal value ln 2. This saturation is a general property of entanglement asymmetry for discrete symmetries reported in Ref. [105], which shows that for a \mathbb{Z}_N symmetry the entanglement asymmetry saturates to $\ln N$ for $\ell \gg 1$. Indeed, since X_0 in Eq. (38) decays exponentially with respect to ℓ , we obtain from Eq. (39) that

$$\lim_{\ell \to \infty} \Delta S_A^{(n)}(0) = H^{(n)}(0) = \ln 2, \tag{43}$$

for $M/J \neq 0$.

We also find in Fig. 4 that the entanglement asymmetry exhibits nonanalytic behavior at M=0 and becomes independent of L_y when L_y is divisible by three. Otherwise, it is smooth around M/J=0 and increases with L_y . This peculiar dependence in the behavior of the entanglement asymmetry on L_y is attributed to the presence of Dirac points in the Brillouin zone: According to Eq. (39), the entanglement asymmetry in the ground state is univocally described by X_0 , which is given in Eq. (38). When L_y is not divisible by three, the quantized momenta ${\bf k}$ cannot take the Dirac points and hence $\varepsilon_{\mathbf{k}} > 0 \ \forall \mathbf{k}$. In this case, the integrand on the right-hand side of Eq. (38) for small M/J can be expanded in terms of $M/\varepsilon_{\mathbf{k}}$ as

$$X_0 \simeq \exp\left(-\frac{\ell M^2}{4\pi} \sum_{n_y=0}^{L_y-1} \int_{-\pi}^{\pi} \frac{dk_x}{\varepsilon_{\mathbf{k}}^2}\right). \tag{44}$$

The above result shows that the entanglement asymmetry in Eq. (39) depends on L_y and is analytic around M/J=0. On the other hand, when L_y is divisible by three, $\varepsilon_{\bf k}$ vanishes at the Dirac points ${\bf k}=\pm(2\pi/3,4\pi/3)$. In this case, since the integrand in Eq. (38) diverges at $\varepsilon_{\bf k}=0$, the summation over n_y is dominated by the terms with $n_y=L_y/3$ and $2L_y/3$, on which the Dirac points appear. Equation (38) can then be approximated as

$$X_0 \simeq \exp\left(-\ell \sum_{k_y = \pm 2\pi/3} \int_{-\pi}^{\pi} \frac{dk_x}{4\pi} \ln\left(1 + \frac{M^2}{\varepsilon_{\mathbf{k}}^2}\right)\right). \tag{45}$$

Observing that the main contribution of the integral in the above equation comes from the vicinity of the Dirac points where $\varepsilon_{\mathbf{k}} \simeq J|k_x \mp 2\pi/3|$ with fixed $k_y = \pm 2\pi/3$, Eq. (45) can be evaluated as

$$X_0 \simeq \exp\left(-\ell \int_{\mathbb{R}} \frac{dk_x}{2\pi} \ln\left(1 + \frac{M^2}{J^2 k_x^2}\right)\right) = e^{-\frac{\ell |M|}{J}}. \quad (46)$$

Here, we extended the integral domain to $k_x \in \mathbb{R}$ using the fact that the integrand in the above expression is suppressed away from the Dirac points. Equation (46) clearly demonstrates that the entanglement asymmetry in Eq. (39) exhibits nonanalytic behavior at M=0 and is independent of L_y . The entanglement asymmetry evaluated with Eqs. (44) and (46) is plotted by the black dashed lines in Fig. 4, showing an excellent agreement with the exact numerical result.

V. QUENCH DYNAMICS OF ENTANGLEMENT ASYMMETRY

In this section, we investigate the time evolution of the inversion-symmetry breaking after the quantum quench starting from $M \neq 0$ into M = 0. We analytically derive the asymptotic form of the entanglement asymmetry in the ballistic limit, $Jt, \ell \to \infty$ with Jt/ℓ fixed, by taking the thermodynamic limit in the longitudinal direction $L_x \to \infty$.

Using the fact that Eqs. (39) and (41) are derived by decomposing the charged moments into independent one-dimensional contributions labeled by $k_y = 2\pi n_y/L_y$, we can extend it to finite times by invoking the quasiparticle picture, which is a semiclassical description for the quench dynamics of one-dimensional integrable systems [37–39]. According to this picture, a global quench at t = 0 uniformly creates quasiparticle excitations throughout the system, and those generated at the same position form entangled pairs that ballistically propagate in time. The ratio $Z_{n,k_y}(\boldsymbol{\alpha},t)/Z_{n,k_y}(\boldsymbol{0},t)$ is then determined by the number of the pairs that remain inside the subsystem, while the integrand $\ln \sin^2 \theta_{\mathbf{k}}$ in Eq. (36) represents the contribution of each quasiparticle mode to the charged moments [40, 41, 45, 48]. The integrand can be expressed by using the correlation function between quasiparticle excitations as

$$\ln \sin^2 \theta_{\mathbf{k}} = \ln(1 - 4|\langle \Psi_0| \gamma_{\mathbf{k}+}^{\dagger} \gamma_{\mathbf{k}-} | \Psi_0 \rangle|^2). \tag{47}$$

Equation (47) suggests that, in our setting, the quasiparticles in the upper and lower bands are excited as the pairs by the quench. Since their dispersion relations are $\pm \varepsilon_{\mathbf{k}}$, their group velocities are opposite, $\pm \partial_{k_x} \varepsilon_{\mathbf{k}}$. As a result, the pairs propagate in the opposite direction after the quench, and the number of the pairs inside the subsystem gradually decreases in time. This effect can be incorporated by replacing the prefactor ℓ in Eq. (36) with $\max(\ell-2|\partial_{k_x}\varepsilon_{\mathbf{k}}|t,0)$ [40, 41, 45, 48]. We then obtain the asymptotic form of the momentum-resolved charged moments in the ballistic limit, $Jt,\ell\to\infty$ with Jt/ℓ fixed, as

$$\ln \frac{Z_{n,k_y}(\boldsymbol{\alpha},t)}{Z_{n,k_y}(\boldsymbol{0},t)} \simeq \ell N^{(n)}(\boldsymbol{\alpha}) \int_{-\pi}^{\pi} \frac{dk_x}{4\pi} x_{\zeta}(\mathbf{k}) \ln \sin^2 \theta_{\mathbf{k}}, \quad (48)$$

where $x_{\zeta}(\mathbf{k}) = \max(1 - 2|\partial_{k_x}\varepsilon_{\mathbf{k}}|\zeta,0)$ denotes the fraction of the pairs with momentum \mathbf{k} that are inside the subsystem at the rescaled time $\zeta = t/\ell$.

Using Eq. (48) and following the same calculation as those in deriving Eq. (39), we obtain the asymptotic form of the entanglement asymmetry after the quench,

$$\Delta S_A^{(n)}(t) \simeq H^{(n)}(X_\zeta),\tag{49}$$

where

$$X_{\zeta} = \exp\left(\ell \sum_{n_y=0}^{L_y-1} \int_{-\pi}^{\pi} \frac{dk_x}{4\pi} x_{\zeta}(\mathbf{k}) \ln \sin^2 \theta_{\mathbf{k}}\right).$$
 (50)

In Figs. 5 (a)-(c), we show the time evolution of the entanglement asymmetry after the quench from the ground state at $M \neq 0$ to M = 0 with several fixed values of L_y and the replica index n. Our analytical result in Eq. (49) agrees excellently with the exact numerical results obtained by using Eq. (29). Notably, the qualitative behavior of the Rényi entanglement asymmetry does not depend on the replica index n.

The lower panels of Figs. 5 (a)-(c) show that, for odd L_y , the entanglement asymmetry tends to zero, suggesting that the inversion symmetry broken in the initial state is restored after the quench. This is consistent with the expectation that the reduced density matrix ρ_A for the subsystem relaxes into its corresponding GGE, $\rho_A(t \to \infty) = \text{Tr}_{\bar{A}}(\rho_{\text{GGE}})$ [18–26], where

$$\rho_{\text{GGE}} = \frac{e^{\sum_{\mathbf{k},s=\pm} \lambda_{\mathbf{k},s} \gamma_{\mathbf{k}s}^{\dagger} \gamma_{\mathbf{k}s}}}{\text{Tr}\left[e^{\sum_{\mathbf{k},s=\pm} \lambda_{\mathbf{k},s} \gamma_{\mathbf{k}s}^{\dagger} \gamma_{\mathbf{k}s}}\right]}.$$
 (51)

Here, $\{\lambda_{\mathbf{k},\pm}\}$ are the Lagrange multipliers determined by the conservation laws,

$$\operatorname{Tr}\left[\rho_{\mathrm{GGE}}\gamma_{\mathbf{k}\pm}^{\dagger}\gamma_{\mathbf{k}\pm}\right] = \langle \Psi_{0}| \gamma_{\mathbf{k}\pm}^{\dagger}\gamma_{\mathbf{k}\pm} |\Psi_{0}\rangle. \tag{52}$$

One readily finds that the GGE respects the inversion symmetry, i.e., $\mathcal{P}\rho_{\text{GGE}}\mathcal{P}^{-1}=\rho_{\text{GGE}}$. Therefore, as the reduced density matrix approaches the GGE, the inversion symmetry broken in the initial state is restored, and

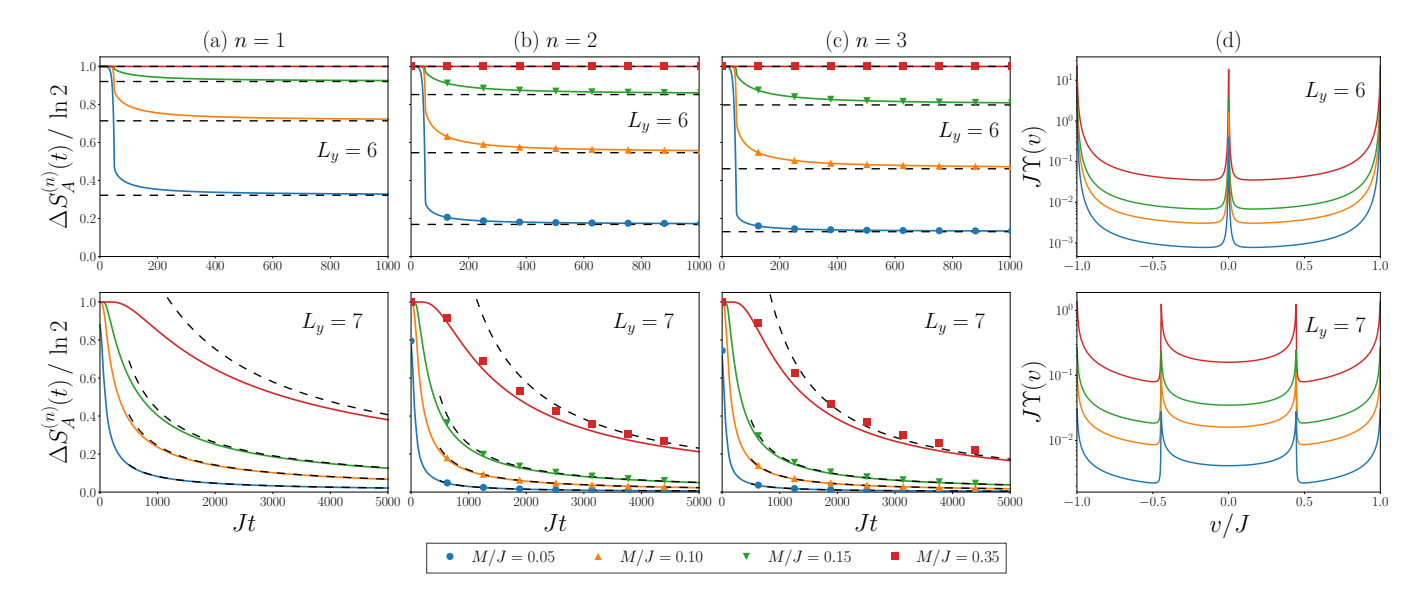


FIG. 5. (a)-(c) Time evolution of the n-th order Rényi entanglement asymmetry after the quench into the Hamiltonian (13) starting from the ground state of the Hamiltonian (1) for several finite M/J values. The solid curves denote the analytical result in Eq. (49) with Eq. (50). The symbols are the exact value of the Rényi entanglement asymmetry obtained by numerically evaluating the charged moments using Eq. (29). The dashed lines correspond to Eqs. (56) and (58) that predict the asymptotic form of the entanglement asymmetry at large times. We take $\ell = 100$ in all the plots. (d) $\Upsilon(v)$ defined in Eq. (54) that characterizes how much the quasiparticle pairs with the longitudinal group velocity v contribute to the entanglement asymmetry. To numerically evaluate $\Upsilon(v)$, we approximate the Dirac delta function in Eq. (54) by the Lorentz function $\delta_{\eta}(x) = \eta/[\pi(x^2 + \eta^2)]$ with $\eta = 10^{-3}$.

the entanglement asymmetry vanishes in the large-time limit. On the other hand, we observe in the upper panels of Figs. 5 (a)-(c) that, when L_y is even, the entanglement asymmetry remains finite even at large times, indicating the absence of symmetry restoration. This result suggests that the reduced density matrix does not relax into the GGE in Eq. (51). We have thus found, both analytically and numerically, that the manner in which the subsystem relaxes critically depends on its geometry.

VI. ABSENCE OF INVERSION-SYMMETRY RESTORATION

In the previous section, we found that the behavior of the entanglement asymmetry after the quench drastically changes depending on the parity of the subsystem size in the transverse direction. In particular, when L_y is even, the entanglement asymmetry does not tend to zero even in the large-time limit $t \to \infty$. That is, the inversion symmetry broken by the initial state is not restored after the quench. In this section, we clarify the physical origin of this anomalous behavior based on the quasiparticle picture.

As shown in Eq. (49), the entanglement asymmetry after the quench is given by X_{ζ} . To deduce the behavior of the entanglement asymmetry at large times, we first

rewrite X_{ζ} in Eq. (50) as

$$X_{\zeta} = \exp\left(-\ell \int_{\mathbb{R}} dv \tilde{x}_{\zeta}(v) \Upsilon(v)\right), \tag{53}$$

where

$$\Upsilon(v) = -\sum_{n_y=0}^{L_y-1} \int_{-\pi}^{\pi} \frac{dk_x}{4\pi} \delta(v - \partial_{k_x} \varepsilon_{\mathbf{k}}) \ln \sin^2 \theta_{\mathbf{k}}.$$
 (54)

Here, $\tilde{x}_{\zeta}(v) = \max(1-2|v|\zeta,0)$ denotes the fraction of quasiparticle pairs with longitudinal velocities $\pm \partial_{k_x} \varepsilon_{\mathbf{k}} = \pm v$ that remain inside the subsystem at the rescaled time $\zeta = t/\ell$, while $\Upsilon(v)$ quantifies the weight of their contribution to the entanglement asymmetry. At time ζ , $\tilde{x}_{\zeta}(v)$ vanishes for $2|v|\zeta>1$, thereby filtering out the contributions of fast-moving quasiparticle pairs that have already escaped from the subsystem. The entanglement asymmetry at large times $\zeta\gg 1$ is therefore governed solely by the slow-moving quasiparticle pairs, whose contributions are given by $\Upsilon(v)$ in the vicinity of v=0.

In Fig. 5 (d), we show the function $\Upsilon(v)$ for the initial states considered in the other panels. To numerically evaluate $\Upsilon(v)$, we replaced the Dirac delta function in Eq. (54) with the Lorentz function $\delta_{\eta}(x) = \eta/[\pi(x^2+\eta^2)]$, which reduces to $\delta(x)$ in the limit $\eta \to 0$. These figures show that $\Upsilon(v)$ exhibits a sharp peak at v = 0 when L_y is even, whereas this peak is absent otherwise. The height of the peak at v = 0 diverges as $\Upsilon(0) \propto \eta^{-1}$, implying that, for even L_y , a macroscopic number of quasiparticle

pairs with zero longitudinal velocity are excited by the quench. Since these pairs never leave the subsystem, the entanglement asymmetry does not tend to zero and the inversion symmetry is not restored, as observed in the upper panels of Figs. 5 (a)-(c).

The divergent peak of $\Upsilon(v)$ at v=0 originates from the fact that, as seen in Fig. 2 (a), the dispersion relation $\varepsilon_{\mathbf{k}}$ becomes independent of k_x at $k_y = \pi$, which occurs only when L_y is even. In other words, all L_x quasiparticle modes with fixed $k_y = \pi$ have zero longitudinal group velocity, resulting in an infinite number of such modes in the thermodynamic limit $L_x \to \infty$. Consequently, their total contribution to the entanglement asymmetry, $\Upsilon(0)$, diverges. We thus find that the absence of inversionsymmetry restoration originates from the presence of the flat energy dispersion with fixed $k_y = \pi$, elucidating the critical role of the band structure and its exotic dispersion on the symmetry restoration. This mechanism of the absence of symmetry restoration is distinct from those reported in previous studies, such as the activation of non-Abelian charges [41] or the Bose-Einstein condensation [62].

In closing this section, we derive explicit expressions for the behavior of the entanglement asymmetry at large times. As argued above, this is governed by $\Upsilon(v)$ in the vicinity of v=0. For odd L_y , expanding $\Upsilon(v)$ in Eq. (53) in terms of v and performing the integral over v, we obtain

$$X_{\zeta} \simeq 1 - \frac{\ell \Upsilon(0)}{2\zeta} + O(\zeta^{-2}). \tag{55}$$

Substituting the above expression into Eq. (49) and expanding it in terms of ζ^{-1} , we obtain

$$\Delta S_A^{(n)}(t) \simeq \frac{\ell \Upsilon(0)}{4\zeta} \times \begin{cases} \frac{n}{n-1} & n \ge 2, \\ \ln \frac{4e\zeta}{\Upsilon(0)\ell} & n \to 1 \end{cases}, \tag{56}$$

for $Jt \gg \ell$. The above expression shows that the entanglement asymmetry tends to zero as $(Jt)^{-1} [(Jt)^{-1} \ln(Jt)]$ when $n \to 1$, indicating that the inversion symmetry broken in the initial state is restored after the quench. In the lower panels of Figs. 5 (a)-(c), we see that Eq. (56) shown as dashed curves well reproduces the long-time asymptotic behavior of the entanglement asymmetry.

For even L_y , the function $x_{\zeta}(\mathbf{k})$ in Eq. (50) vanishes except for $k_y = \pi$, where it reduces to unity because $\partial_{k_x} \varepsilon_{\mathbf{k}}|_{k_y=\pi} = 0$, at large times. This allows us to replace $x_{\zeta}(\mathbf{k})$ in Eq. (50) with $\delta_{k_y,\pi}$, which results in

$$X_{\zeta} \simeq [1 + (M/J)^2]^{-\ell/2} + O(\zeta^{-1}).$$
 (57)

Here, we used $\varepsilon_{\mathbf{k}}|_{k_y=\pi}=J$. Substituting Eq. (57) into Eq. (49), we obtain the saturation value of the entanglement asymmetry in the large-time limit as

$$\lim_{t \to \infty} \Delta S_A^{(n)}(t) = H^{(n)}([1 + (M/J)^2]^{-\ell/2}).$$
 (58)

As shown in the upper panels of Figs. 5 (a)-(c), this expression excellently agrees with the saturation value of the entanglement asymmetry. Furthermore, combining Eq. (58) with Eq. (43), we obtain

$$\lim_{\ell \to \infty} \Delta S_A^{(n)}(0) = \lim_{\ell \to \infty} \Delta S_A^{(n)}(\infty) = \ln 2.$$
 (59)

This means that, despite the symmetric dynamics, the inversion symmetry broken in the initial state remains intact throughout the time evolution, owing to the macroscopic occupation of quasiparticle modes with zero longitudinal velocity. As shown by the red squares in the upper panels of Figs. 5 (a)-(c), this effect is visible even for finite ℓ . This suggests that the absence of symmetry restoration can be observed even for a relatively small-sized system, opening the door for testing our prediction in cold atom experiments [85–87].

VII. CONCLUSION

We have investigated the space-inversion symmetry within a subsystem of free fermions on a honeycomb lattice. By computing the entanglement asymmetry analytically and numerically, we demonstrated that the subsystem geometry and the band structure play crucial roles in symmetry breaking both in and out of equilibrium.

In the ground state, the entanglement asymmetry exhibits a nonanalytic dependence on the sublattice imbalance M when the transverse subsystem size L_y is multiple of three, where the quantized momenta can take the Dirac points. For the quench dynamics from $M \neq 0$ to M = 0, the parity of L_y governs whether the inversion symmetry is restored or remains broken: For odd L_y , the inversion symmetry is restored as the subsystem relaxes into the symmetric GGE. In contrast, for even L_y , a flat dispersion with a fixed transverse momentum leads to a macroscopic occupation of quasiparticle modes with zero group velocity, which prevents the subsystem from relaxing and restoring the symmetry.

Our quench protocol can be realized in cold atoms in optical lattices [85–87], where both the lattice geometry and the energy imbalance can be precisely controlled. In such setups, the n=2 Rényi entanglement asymmetry is expected to be experimentally accessible by combining the beam-splitter interference with the site-resolved imaging, which may enable the direct measurement of the charged moment [9, 32, 101, 102]. Experimentally verifying our predictions would provide valuable insights into the connections between relaxation dynamics, system geometry, and band structure.

ACKNOWLEDGMENTS

We thank Filiberto Ares and Soma Takemori for fruitful discussions. SY was supported by Grant-in-Aid for Young Scientists (Start-up) No. 25K23355 and

Institute for Advanced Science, University of Electro-Communications. SE acknowledges support from JSPS KAKENHI Grant Numbers JP23H01174, JP25K00217, Matsuo Foundation, and Institute for Advanced Science, University of Electro-Communications.

Appendix A: Derivation of Eq. (24)

In this appendix, we derive Eq. (24). To this end, we need to compute the trace of the product of ρ_{A,α_j} which are given in Eq. (23). Applying the Baker-Campbell-Hausdorff formula and using the following commutation relation for arbitrary matrices A and B,

$$\left[\sum_{\mathbf{i},\mathbf{j}\in A\cup\Lambda_{A}} \mathbf{\Psi}_{\mathbf{i}}^{\dagger} A_{\mathbf{i},\mathbf{j}} \mathbf{\Psi}_{\mathbf{j}}, \sum_{\mathbf{i}',\mathbf{j}'\in A\cup\Lambda_{A}} \mathbf{\Psi}_{\mathbf{i}'}^{\dagger} B_{\mathbf{i}',\mathbf{j}'} \mathbf{\Psi}_{\mathbf{j}'} \right] \\
= \sum_{\mathbf{i},\mathbf{j}\in A\cup\Lambda_{A}} \mathbf{\Psi}_{\mathbf{i}}^{\dagger} [A,B]_{\mathbf{i},\mathbf{j}} \mathbf{\Psi}_{\mathbf{j}}, \quad (A1)$$

we can express the product of ρ_{A,α_i} as

$$\prod_{j=1}^{n} \rho_{A,\alpha_{j}} = \det \left[\prod_{j=1}^{n} \frac{I + \Gamma_{\alpha_{j}}}{2} \right] \times \exp \left(\sum_{\mathbf{i},\mathbf{i}' \in A \cap \Lambda_{A}} \Psi_{\mathbf{i}}^{\dagger} K(\boldsymbol{\alpha})_{\mathbf{i},\mathbf{i}'} \Psi_{\mathbf{i}'} \right), \quad (A2)$$

where

$$K(\boldsymbol{\alpha}) = \log \left(\prod_{j=1}^{n} \frac{I - \Gamma_{\alpha_j}}{I + \Gamma_{\alpha_j}} \right).$$
 (A3)

Since the exponent on the right-hand side of Eq. (A2) is quadratic in Ψ_i , it can be diagonalized as

$$\prod_{j=1}^{n} \rho_{A,\alpha_{j}} = \det \left(\prod_{j=1}^{n} \frac{I + \Gamma_{\alpha_{j}}}{2} \right) e^{\sum_{i=1}^{2\ell L_{y}} \omega_{i} \gamma_{i}^{\dagger} \gamma_{i}}, \quad (A4)$$

where ω_i is the *i*-th eigenvalue of $K(\boldsymbol{\alpha})$ and γ_i (γ_i^{\dagger}) is a fermionic annihilation (creation) operator. Taking the trace of Eq. (A4), we obtain

$$Z_n(\boldsymbol{\alpha}, t) = \det \left[\prod_{j=1}^n \frac{I + \Gamma_{\alpha_j}}{2} \right] \prod_{j=1}^{2\ell L_y} (1 + e^{\omega_i})$$

$$= \det \left[\prod_{j=1}^n \frac{I + \Gamma_{\alpha_j}}{2} \right] \det \left[I + e^{K(\boldsymbol{\alpha})} \right].$$
 (A6)

Substituting Eq. (A3) into Eq. (A6), we arrive at Eq. (24).

Appendix B: Derivation of Eqs. (36)

Here, we derive Eq. (36) from Eq. (29), which involves products and inverses of the block-Toeplitz matrices $I \pm \Gamma_{\alpha,k_y}$. As discussed in Sec. IV, for $\ell \gg 1$, the multiple of the block-Toeplitz matrices can be approximated by the block-Toeplitz matrix generated by the product of the symbols of the factors. Namely, if we denote as $T[\mathcal{G}]$ the $2\ell \times 2\ell$ block-Toeplitz matrix generated by the two-dimensional symbol \mathcal{G} , the following approximation holds for $\ell \gg 1$,

$$T[\mathcal{G}]T[\mathcal{G}'] \simeq T[\mathcal{G}\mathcal{G}'].$$
 (B1)

Substituting \mathcal{G}^{-1} into \mathcal{G}' in the above equation, we obtain

$$T[\mathcal{G}]^{-1} \simeq T[\mathcal{G}^{-1}]. \tag{B2}$$

Using Eqs. (B1) and (B2), the charged moments in Eq. (29) at t=0 can be approximated as

$$\ln Z_{n,k_y}(\boldsymbol{\alpha},0) \simeq \lim_{c \to 1} \det T[z_{n,\mathbf{k},c}(\boldsymbol{\alpha})],$$
 (B3)

where

$$z_{n,\mathbf{k},c}(\boldsymbol{\alpha}) = \prod_{j=1}^{n} \frac{I + c \,\mathcal{G}_{\mathbf{k},\alpha_{j}}(0)}{2} \times \left[I + \prod_{j=1}^{n} \frac{I - c \,\mathcal{G}_{\mathbf{k},\alpha_{j}}(0)}{I + c \,\mathcal{G}_{\mathbf{k},\alpha_{j}}(0)} \right]. \quad (B4)$$

Here, we introduced constant c to avoid the singularity of $(I + \mathcal{G}_{\mathbf{k},\alpha_j})^{-1}$. Applying Widom-Szegő theorem [104] to Eq. (B3), we obtain

$$\ln \frac{Z_{n,k_y}(\boldsymbol{\alpha},0)}{Z_{n,k_y}(\boldsymbol{0},0)} \simeq \lim_{c \to 1} \ell \int_{-\pi}^{\pi} \frac{dk_x}{2\pi} \ln \det z_{n,\mathbf{k},c}(\boldsymbol{\alpha}). \quad (B5)$$

Here, we used $\det[z_{n,\mathbf{k},c}(\mathbf{0})] = 1$.

Using Eq. (B4), the integrand on the right-hand side of Eq. (B5) can be written as

$$\ln \det z_{n,\mathbf{k},c}(\boldsymbol{\alpha}) = \ln \prod_{j=1}^{n} \det \frac{I + c \,\mathcal{G}_{\mathbf{k},\alpha_{j}}(0)}{2} + \ln \det \left[I + \prod_{j=1}^{n} \frac{I - c \,\mathcal{G}_{\mathbf{k},\alpha_{j}}(0)}{I + c \,\mathcal{G}_{\mathbf{k},\alpha_{j}}(0)} \right]. \quad (B6)$$

Since $I + c \mathcal{G}_{\mathbf{k},\alpha_j}$ has eigenvalues $1 \pm c$, the first term on the right-hand side of Eq. (B6) reduces to

$$\ln \prod_{j=1}^{n} \det \frac{I + c \mathcal{G}_{\mathbf{k},\alpha_{j}}(0)}{2} = n \ln \left(\frac{1 - c^{2}}{4}\right).$$
 (B7)

To evaluate the second term on the right-hand side of Eq. (B6), we use the following formula for any 2×2 matrices A and B,

$$\det(A+B) = \det A + \det B + \operatorname{Tr} A \operatorname{Tr} B - \operatorname{Tr} AB.$$
 (B8)

Applying Eq. (B7) and the above formula to the first and the second terms on the right-hand side of Eq. (B6), respectively, we obtain

$$\ln \det z_{n,\mathbf{k},c}(\boldsymbol{\alpha}) = n \ln \left(\frac{1 - c^2}{4} \right) + \ln \left(2 + \operatorname{Tr} \prod_{j=1}^{n} \frac{I - c \, \mathcal{G}_{\mathbf{k},\alpha_j}(0)}{I + c \, \mathcal{G}_{\mathbf{k},\alpha_j}(0)} \right).$$
(B9)

Here, we used

$$\det\left(\prod_{j=1}^{n} \frac{I - c \mathcal{G}_{\mathbf{k},\alpha_{j}}(0)}{I + c \mathcal{G}_{\mathbf{k},\alpha_{j}}(0)}\right) = 1,$$
 (B10)

which can be readily derived from the fact that $I + c \mathcal{G}_{\mathbf{k},\alpha_i}$ has eigenvalues of $1 \pm c$. Using the identity

$$\left(I + c \mathcal{G}_{\mathbf{k},\alpha_j}(0)\right)^{-1} = \frac{I - c \mathcal{G}_{\mathbf{k},\alpha_j}(0)}{1 - c^2}, \tag{B11}$$

Eq. (B9) reduces to

$$\ln \det z_{n,\mathbf{k},c}(\boldsymbol{\alpha}) = n \ln \left(\frac{1-c^2}{4} \right) + \ln \left(2 + \frac{\operatorname{Tr} \prod_{j=1}^{n} (I - c \mathcal{G}_{\mathbf{k},\alpha_j}(0))^2}{(1-c^2)^n} \right).$$
(B12)

Substituting it into Eq. (B5) and taking the limit $c \to 1$, we obtain

$$\ln \frac{Z_{n,k_y}(\boldsymbol{\alpha},0)}{Z_{n,k_y}(\boldsymbol{0},0)} \simeq \ell \int_{-\pi}^{\pi} \frac{dk_x}{2\pi} \ln \operatorname{Tr} \prod_{j=1}^{n} \frac{I - \mathcal{G}_{\mathbf{k},\alpha_j}(0)}{2}.$$
(B13)

Substituting Eq. (22) into Eq. (B13) and using the cyclic property of trace, we obtain

$$\ln \frac{Z_{n,k_y}(\boldsymbol{\alpha},0)}{Z_{n,k_y}(\boldsymbol{0},0)} \simeq \ell \int_{-\pi}^{\pi} \frac{dk_x}{2\pi} \ln \operatorname{Tr} \prod_{j=1}^{n} \Pi_{\mathbf{k}} \sigma_x^{\alpha_j - \alpha_{j+1}}, \text{ (B14)}$$

where

$$\Pi_{\mathbf{k}} = \frac{I - \sigma_x \sin \theta_{\mathbf{k}} - \sigma_z \cos \theta_{\mathbf{k}}}{2}.$$
 (B15)

[1] A. Polkovnikov, K. Sengupta, A. Silva, and M. Ven-

By simple algebra, one finds that $\Pi_{\mathbf{k}} \sigma_x^{\alpha_j - \alpha_{j+1}} \Pi_{\mathbf{k}} = \Pi_{\mathbf{k}}$ if $\alpha_j = \alpha_{j+1}$. This allows us to rewrite Eq. (B14) as

$$\ln \frac{Z_{n,k_y}(\boldsymbol{\alpha},0)}{Z_{n,k_y}(\boldsymbol{0},0)} \simeq \ell \int_{-\pi}^{\pi} \frac{dk_x}{2\pi} \ln \text{Tr}\Big[(\Pi_{\mathbf{k}} \sigma_x)^{N^{(n)}(\boldsymbol{\alpha})} \Big], \text{ (B16)}$$

where $N^{(n)}(\boldsymbol{\alpha}) = \sum_{j=1}^{n} |\alpha_j - \alpha_{j+1}|$ counts the number of domain walls, at which $\alpha_j \neq \alpha_{j+1}$, in the bit string $\alpha \in \{0,1\}^n$. Using the fact that the matrix $\Pi_{\mathbf{k}}\sigma_x$ has the eigenvalues $-\sin\theta_{\mathbf{k}}$ and 0, we obtain $\mathrm{Tr}[(\Pi_{\mathbf{k}}\sigma_x)^m] =$ $(-\sin\theta_{\mathbf{k}})^m$. The right-hand side of Eq. (B16) can therefore be rewritten as

$$\ln \frac{Z_{n,k_y}(\boldsymbol{\alpha},0)}{Z_{n,k_y}(\boldsymbol{0},0)} \simeq \ell N^{(n)}(\boldsymbol{\alpha}) \int_{-\pi}^{\pi} \frac{dk_x}{4\pi} \ln \sin^2 \theta_{\mathbf{k}}, \quad (B17)$$

which corresponds to Eq. (36) in the main text.

Appendix C: Derivation of Eq. (39)

Here, we give the derivation of Eq. (39). Substituting Eq. (37) into Eq. (18), we have

$$\Delta S_A^{(n)}(0) = \frac{1}{1-n} \ln \left(\frac{1}{2^n} \sum_{\alpha \in \{0,1\}^n} X_0^{N^{(n)}(\alpha)} \right). \quad (C1)$$

Recalling that $N^{(n)}(\boldsymbol{\alpha}) = \sum_{j=1}^{n} |\alpha_j - \alpha_{j+1}|$ counts the number of domain walls between regions of consecutive 0's and 1's in the bit string $\alpha = (\alpha_1, \alpha_2, ..., \alpha_n)$ $(\alpha_i \in$ $\{0,1\}$), the summation over α in the above equation can be rewritten as

$$\Delta S_A^{(n)}(0) = \frac{1}{1-n} \ln \left(\frac{1}{2^n} \sum_{m=0}^{\lfloor \frac{n}{2} \rfloor} {n \choose 2m} X_0^{2m} \right).$$
 (C2)

Here, the binomial coefficient on the right-hand side represents the number of all possible bit strings α that have 2m domain walls. Performing the summation over m, we obtain Eq. (39).

galattore, Reviews of Modern Physics 83, 863 (2011). [2] J. Eisert, M. Friesdorf, and C. Gogolin, Nature Physics **11**, 124 (2015).

^[3] L. D'Alessio, Y. Kafri, A. Polkovnikov, and M. Rigol, Advances in Physics **65**, 239 (2016).

^[4] F. Borgonovi, F. M. Izrailev, L. F. Santos, and V. G. Zelevinsky, Physics Reports 626, 1 (2016).

^[5] J. M. Deutsch, Physical Review A 43, 2046 (1991).

^[6] M. Srednicki, Physical Review E 50, 888 (1994).

^[7] M. Srednicki, Journal of Physics A: Mathematical and General **32**, 1163 (1999).

^[8] M. Rigol, V. Dunjko, and M. Olshanii, Nature 452, 854

A. M. Kaufman, M. E. Tai, A. Lukin, M. Rispoli, R. Schittko, P. M. Preiss, and M. Greiner, Science 353,

- 794 (2016).
- [10] H. Tasaki, Physical Review Letters 80, 1373 (1998).
- [11] S. Popescu, A. J. Short, and A. Winter, Nature Physics 2, 754 (2006).
- [12] S. Goldstein, J. L. Lebowitz, R. Tumulka, and N. Zanghì, Physical Review Letters 96, 050403 (2006).
- [13] P. Reimann, Physical Review Letters 101, 190403 (2008).
- [14] N. Linden, S. Popescu, A. J. Short, and A. Winter, Physical Review E 79, 061103 (2009).
- [15] A. J. Short and T. C. Farrelly, New Journal of Physics 14, 013063 (2012).
- [16] P. Reimann and M. Kastner, New Journal of Physics 14, 043020 (2012).
- [17] C. Gogolin and J. Eisert, Reports on Progress in Physics 79, 056001 (2016).
- [18] M. Rigol, V. Dunjko, V. Yurovsky, and M. Olshanii, Physical Review Letters 98, 050405 (2007).
- [19] J.-S. Caux and F. H. Essler, Physical Review Letters 110, 257203 (2013).
- [20] E. Ilievski, J. De Nardis, B. Wouters, J.-S. Caux, F. H. Essler, and T. Prosen, Physical Review Letters 115, 157201 (2015).
- [21] L. Vidmar and M. Rigol, Journal of Statistical Mechanics: Theory and Experiment 2016, 064007 (2016).
- [22] F. H. Essler and M. Fagotti, Journal of Statistical Mechanics: Theory and Experiment 2016, 064002 (2016).
- [23] T. Langen, S. Erne, R. Geiger, B. Rauer, T. Schweigler, M. Kuhnert, W. Rohringer, I. E. Mazets, T. Gasenzer, and J. Schmiedmayer, Science 348, 207 (2015).
- [24] T. Barthel and U. Schollwöck, Physical Review Letters 100, 100601 (2008).
- [25] M. Cramer, C. M. Dawson, J. Eisert, and T. J. Osborne, Physical Review Letters 100, 030602 (2008).
- [26] P. Calabrese, F. H. Essler, and M. Fagotti, Journal of Statistical Mechanics: Theory and Experiment 2012, P07022 (2012).
- [27] B. Neyenhuis, J. Zhang, P. W. Hess, J. Smith, A. C. Lee, P. Richerme, Z.-X. Gong, A. V. Gorshkov, and C. Monroe, Science advances 3, e1700672 (2017).
- [28] T. Brydges, A. Elben, P. Jurcevic, B. Vermersch, C. Maier, B. P. Lanyon, P. Zoller, R. Blatt, and C. F. Roos, Science 364, 260 (2019).
- [29] H. B. Kaplan, L. Guo, W. L. Tan, A. De, F. Marquardt, G. Pagano, and C. Monroe, Physical Review Letters 125, 120605 (2020).
- [30] T. Kinoshita, T. Wenger, and D. S. Weiss, Nature 440, 900 (2006).
- [31] M. Cheneau, P. Barmettler, D. Poletti, M. Endres, P. Schauß, T. Fukuhara, C. Gross, I. Bloch, C. Kollath, and S. Kuhr, Nature 481, 484 (2012).
- [32] R. Islam, R. Ma, P. M. Preiss, M. Eric Tai, A. Lukin, M. Rispoli, and M. Greiner, Nature 528, 77 (2015).
- [33] L. Amico, R. Fazio, A. Osterloh, and V. Vedral, Reviews of Modern Physics 80, 517 (2008).
- [34] J. Eisert, M. Cramer, and M. B. Plenio, Reviews of Modern Physics 82, 277 (2010).
- [35] P. Calabrese, J. Cardy, and B. Doyon, Journal of Physics A: Mathematical and Theoretical 42, 500301 (2009).
- [36] N. Laflorencie, Physics Reports **646**, 1 (2016).
- [37] P. Calabrese and J. Cardy, Journal of Statistical Mechanics: Theory and Experiment 2005, P04010 (2005).
- [38] M. Fagotti and P. Calabrese, Physical Review A 78, 010306 (2008).

- [39] V. Alba and P. Calabrese, Proceedings of the National Academy of Sciences 114, 7947 (2017).
- [40] F. Ares, S. Murciano, and P. Calabrese, Nature Communications 14, 2036 (2023).
- [41] S. Murciano, F. Ares, I. Klich, and P. Calabrese, Journal of Statistical Mechanics: Theory and Experiment 2024, 013103 (2024).
- [42] S. Yamashika, F. Ares, and P. Calabrese, Physical Review B 110, 085126 (2024).
- [43] S. Liu, H.-K. Zhang, S. Yin, and S.-X. Zhang, Physical Review Letters 133, 140405 (2024).
- [44] K. Chalas, F. Ares, C. Rylands, and P. Calabrese, Journal of Statistical Mechanics: Theory and Experiment 2024, 103101 (2024).
- [45] F. Caceffo, S. Murciano, and V. Alba, Journal of Statistical Mechanics: Theory and Experiment 2024, 063103 (2024).
- [46] C. Rylands, E. Vernier, and P. Calabrese, Journal of Statistical Mechanics: Theory and Experiment 2024, 123102 (2024).
- [47] L. K. Joshi, J. Franke, A. Rath, F. Ares, S. Murciano, F. Kranzl, R. Blatt, P. Zoller, B. Vermersch, P. Calabrese, et al., Physical Review Letters 133, 010402 (2024).
- [48] C. Rylands, K. Klobas, F. Ares, P. Calabrese, S. Murciano, and B. Bertini, Physical Review Letters 133, 010401 (2024).
- [49] F. Ares, V. Vitale, and S. Murciano, Physical Review B 111, 104312 (2025).
- [50] G. Di Giulio, X. Turkeshi, and S. Murciano, Entropy 27, 407 (2025).
- [51] T. Banerjee, S. Das, and K. Sengupta, SciPost Physics 19, 051 (2025).
- [52] X. Turkeshi, P. Calabrese, and A. De Luca, Physical Review Letters 135, 040403 (2025).
- [53] K. Klobas, C. Rylands, and B. Bertini, Physical Review B 111, L140304 (2025).
- [54] H. Yu, Z.-X. Li, and S.-X. Zhang, Chinese Physics Letters (2025).
- [55] Y.-H. Yu, T.-R. Jin, L. Zhang, K. Xu, and H. Fan, Physical Review B 112, 094315 (2025).
- [56] S. Yamashika and F. Ares, arXiv:2507.06636.
- [57] Y. Xu, C.-P. Fang, B.-J. Chen, M.-C. Wang, Z.-Y. Ge, Y.-H. Shi, Y. Liu, C.-L. Deng, K. Zhao, Z.-H. Liu, et al., arXiv:2508.07707.
- [58] H. Yu, S. Liu, and S.-X. Zhang, AAPPS Bulletin 35, 17 (2025).
- [59] F. Ares, P. Calabrese, and S. Murciano, Nature Reviews Physics 7, 451 (2025).
- [60] G. Teza, J. Bechhoefer, A. Lasanta, O. Raz, and M. Vucelja, arXiv:2502.01758.
- [61] F. Ares, S. Murciano, E. Vernier, and P. Calabrese, Sci-Post Physics 15, 089 (2023).
- [62] S. Yamashika, P. Calabrese, and F. Ares, Physical Review A 111, 043304 (2025).
- [63] L. Capizzi and V. Vitale, Journal of Physics A: Mathematical and Theoretical 57, 45LT01 (2024).
- [64] M. Mazzoni, L. Capizzi, and L. Piroli, arXiv:2508.15892.
- [65] M. Fossati, F. Ares, J. Dubail, and P. Calabrese, Journal of High Energy Physics 2024, 1 (2024).
- [66] M. Chen and H.-H. Chen, Physical Review D 109, 065009 (2024).
- [67] Y. Kusuki, S. Murciano, H. Ooguri, and S. Pal, Journal of High Energy Physics 2025, 1 (2025).

- [68] M. Fossati, C. Rylands, and P. Calabrese, Journal of High Energy Physics 2025, 1 (2025).
- [69] F. Ares, S. Murciano, L. Piroli, and P. Calabrese, Physical Review D 110, L061901 (2024).
- [70] S. Yamashika, F. Ares, and P. Calabrese, Physical Review B 109, 125122 (2024).
- [71] M. Gibbins, A. Jafarizadeh, A. Gammon-Smith, and B. Bertini, Physical Review B 109, 224310 (2024).
- [72] R. Travaglino, C. Rylands, and P. Calabrese, Journal of Statistical Mechanics: Theory and Experiment 2025, 033102 (2025).
- [73] A. Russotto, F. Ares, and P. Calabrese, Journal of High Energy Physics 2025, 1 (2025).
- [74] M. Gibbins, A. Smith, and B. Bertini, arXiv:2506.14555.
- [75] F. Benini, P. Calabrese, M. Fossati, A. H. Singh, and M. Venuti, arXiv:2509.16311.
- [76] S. A. Ahmad, M. S. Klinger, and Y. Wang, arXiv:2509.18072.
- [77] A. H. Castro Neto, F. Guinea, N. M. Peres, K. S. Novoselov, and A. K. Geim, Reviews of Modern Physics 81, 109 (2009).
- [78] P. R. Wallace, Physical Review 71, 622 (1947).
- [79] G. W. Semenoff, Physical Review Letters 53, 2449 (1984).
- [80] K. S. Novoselov, A. K. Geim, S. V. Morozov, D. Jiang, M. I. Katsnelson, I. V. Grigorieva, S. V. Dubonos, and A. A. Firsov, Nature 438, 197 (2005).
- [81] Y. Zhang, Y.-W. Tan, H. L. Stormer, and P. Kim, Nature 438, 201 (2005).
- [82] M. Z. Hasan and C. L. Kane, Reviews of Modern Physics 82, 3045 (2010).
- [83] X.-L. Qi and S.-C. Zhang, Reviews of Modern Physics 83, 1057 (2011).
- [84] M. Goerbig, Reviews of Modern Physics 83, 1193 (2011).
- [85] L. Tarruell, D. Greif, T. Uehlinger, G. Jotzu, and T. Esslinger, Nature 483, 302 (2012).
- [86] T. Uehlinger, G. Jotzu, M. Messer, D. Greif, W. Hofstetter, U. Bissbort, and T. Esslinger, Physical Review Letters 111, 185307 (2013).
- [87] G. Jotzu, M. Messer, R. Desbuquois, M. Lebrat, T. Uehlinger, D. Greif, and T. Esslinger, Nature 515, 237 (2014).
- [88] T. Jacqmin, I. Carusotto, I. Sagnes, M. Abbarchi, D. Solnyshkov, G. Malpuech, E. Galopin, A. Lemaître,

- J. Bloch, and A. Amo, Physical Review Letters **112**, 116402 (2014).
- [89] Y. Plotnik, M. C. Rechtsman, D. Song, M. Heinrich, J. M. Zeuner, S. Nolte, Y. Lumer, N. Malkova, J. Xu, A. Szameit, et al., Nature Materials 13, 57 (2014).
- [90] L. Lu, J. D. Joannopoulos, and M. Soljačić, Nature photonics 8, 821 (2014).
- [91] T. Ozawa, H. M. Price, A. Amo, N. Goldman, M. Hafezi, L. Lu, M. C. Rechtsman, D. Schuster, J. Simon, O. Zilberberg, et al., Reviews of Modern Physics 91, 015006 (2019).
- [92] T. Kariyado and Y. Hatsugai, Scientific reports 5, 18107 (2015).
- [93] L. M. Nash, D. Kleckner, A. Read, V. Vitelli, A. M. Turner, and W. T. Irvine, Proceedings of the National Academy of Sciences 112, 14495 (2015).
- [94] Z. Ma, C. Han, Y. Meir, and E. Sela, Physical Review A 105, 042416 (2022).
- [95] C. Han, Y. Meir, and E. Sela, Physical Review Letters 130, 136201 (2023).
- [96] M.-C. Chung and I. Peschel, Physical Review B 62, 4191 (2000).
- [97] F. Ares, J. G. Esteve, F. Falceto, and E. Sánchez-Burillo, Journal of Physics A: Mathematical and Theoretical 47, 245301 (2014).
- [98] S. Murciano, P. Ruggiero, and P. Calabrese, Journal of Statistical Mechanics: Theory and Experiment 2020, 083102 (2020).
- [99] I. Frérot and T. Roscilde, Physical Review Letters 116, 190401 (2016).
- [100] I. Frérot and T. Roscilde, Physical Review B 92, 115129 (2015).
- [101] H. Pichler, L. Bonnes, A. J. Daley, A. M. Läuchli, and P. Zoller, New Journal of Physics 15, 063003 (2013).
- [102] E. Cornfeld, E. Sela, and M. Goldstein, Physical Review A 99, 062309 (2019).
- [103] I. Peschel, Journal of Physics A: Mathematical and General 36, L205 (2003).
- [104] H. Widom, Advances in Mathematics 13, 284 (1974).
- [105] F. Ferro, F. Ares, and P. Calabrese, Journal of Statistical Mechanics: Theory and Experiment 2024, 023101 (2024).